Three-dimensional stability, receptivity and sensitivity of non-Newtonian flows inside open cavities

Vincenzo Citro[1], Flavio Giannetti[1] and Jan O Pralits[2]

[1] DIIN, University of Salerno, Via Ponte don Melillo, 84084 Fisciano (SA), Italy
[2] DICCA, University of Genoa, Via Montallegro 1, 16145 Genoa (GE), Italy

E-mail: vcitro@unisa.it

Abstract

We investigate the stability properties of flows over an open square cavity for fluids with shear-dependent viscosity. Analysis is carried out in context of the linear theory using a normal-mode decomposition. The incompressible Cauchy equations, with a Carreau viscosity model, are discretized with a finite-element method. The characteristics of direct and adjoint eigenmodes are analyzed and discussed in order to understand the receptivity features of the flow. Furthermore, we identify the regions of the flow that are more sensitive to spatially localized feedback by building a spatial map obtained from the product between the direct and adjoint eigenfunctions. Analysis shows that the first global linear instability of the steady flow is a steady or unsteady three-dimensionl bifurcation depending on the value of the power-law index n. The instability mechanism is always located inside the cavity and the linear stability results suggest a strong connection with the classical lid-driven cavity problem.

(Some figures may appear in colour only in the online journal)

1. Introduction

Our notion about the dynamics of many flow configurations are often based on familiar Newtonian fluids such as water and air. The non-Newtonian fluid mechanics, however, can be a very important and useful field because such kinds of flows are often encountered in nature and many industrial applications, where the observed flow can be markedly different from that of its Newtonian counterpart. In this paper we focus our attention on the class of non-Newtonian fluids characterized by an instantaneous mutual relation between the rate of shear and the shear stress. In other words, such fluids have no memory of their past history.

1.1. Shear-thinning and shear-thickening fluids: the Carreau viscosity model

The shear-thinning phenomena are perhaps the most widely encountered type of time-independent non-Newtonian behavior in engineering practice. They are characterized by an apparent viscosity which gradually decreases as the shear rate increases. On the contrary, the shear-thickening fluids present an apparent viscosity that increases with the increasing of the shear rate and hence the characteristic name *dilatant flows*.

In the last century many mathematical equations and models of varying complexity and forms have been reported in the literature; some of these are straightforward attempts to fit the experimental data, while others have a theoretical basis in statistical mechanics (see e.g. Carreau *et al* (1997)). In this work we have chosen to use the Carreau viscosity model, that is based on a molecular theory (Lodge's theory) since it allows to satisfactorily describe the complex behaviors of such fluids. Moreover, it has been widely used to model non-Newtonian fluids (including for example hemodynamic studies, see Hsu *et al* (2009)), and thereby offers the possibility to validate our numerical code.

1.2. Open-cavity instabilities

The open cavity flow is a problem of great interest in many engineering applications such as military aircraft, sunroofs in automobiles or the gap between train wagons. Historically it has been given great attention since it represents a prototype problem in which there is a finite region of separated flow. Rossiter (1964) was the first to give a significant contribution to explain the unsteadiness of flows over rectangular cavities, identifying an acoustic feedback mechanism for cavities of several aspect ratios L/D (i.e. length to depth) and flow regimes. The presence of this Rossiter mode, in turn, generates self-sustained oscillations of velocity, pressure, and, in some cases, density, which may induce strong vibrations in the substrate over which the fluid is flowing. The latter may give rise to structural fatigue or acoustic noise. Many experimental and numerical studies have shown that this resonance is based on a feedback mechanism, whereby small disturbances in the shear layer are amplified by the Kelvin–Helmholtz instability (see e.g. Rowley *et al* (2002)).

However, when significant interactions between the shear layer and the flow within the cavity exist, the flow may be found in a completely different state from that of the cavity resonance that can be described with the aid of the Rossiter model (or any of its improved versions). The resultant mode appears to be a global instability whose frequency of oscillation is independent of the Mach number. Recently, Brés and Colonius (2008) have performed several 3D simulations that have proved, for the first time, the existence of 3D instabilities situated inside the cavity. They showed also that these 3D instabilities are related to centrifugal instabilities previously reported in flows over backward-facing steps, lid-driven cavity flows and Couette flows.

In the field of inelastic non-Newtonian fluids, there are only a few studies aimed at detecting the instability mechanism in the configuration under investigation. One relevant numerical and experimental investigation was reported by Cochrane *et al* (1981). They studied the behavior of the non-Newtonian (PAC) flow and the Newtonian flow (syrup-water mixture) past a square open cavity.

1.3. Goal of present work

The aim of the present work is to study the effects of shear-dependent viscosity on the instability features in incompressible open cavity flows. The goal is to provide a better description of the instability mechanism of 3D perturbations and to show that the instability is
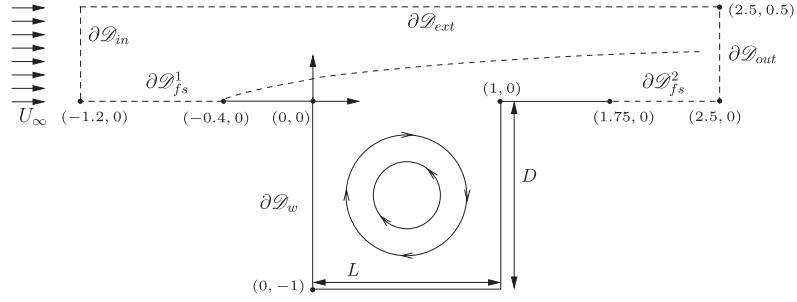
Figure 1. Flow configuration, frame of reference and the computational domain $\mathscr{D}$. The figure also shows a sketched schematic visualization of the base flow structure.

strictly correlated with the one arising in the lid-driven cavity flow. First of all, we perform an accurate analysis of the occurrence of the first instability using the linear stability theory; the critical Reynolds number Re_{cr} and the corresponding spanwise wavenumber, here denoted as the optimal spanwise wavenumber β_{opt}, are computed for different non-Newtonian fluids (i.e. for every couple of parameters n, λ of the Carreau model). After the identification of the first instability, we analyze the adjoint field in order to describe the receptivity behavior.

Furthermore, we determine the instability core by performing a structural sensitivity analysis, as discussed by Chomaz (2005), Giannetti and Luchini (2007) and Marquet *et al* (2008). The spatial map of the structural sensitivity gives a better understanding of the instability mechanism. In the present work, since the flow is globally unstable, we do not consider the sensitivity to transient disturbance growth as considered by Brandt *et al* (2011). Finally, we want to remark that the current sensitivity analysis is not directly applicable when it concerns passive control devices with the scope of controlling instability. In order to do so one must extend the current analysis the include variations of the basic flow. Examples of this can be found in Pralits *et al* (2010) and Pralits *et al* (2013).

2. Theoretical framework

We investigate the stability characteristics of non-Newtonian fluids in the case of a two-dimensionl (2D) flow arising over a square open cavity due to a uniform stream. The geometry, frame of reference and notation are shown in figure 1. A Cartesian system is located on the left edge of the cavity with the *x*-axis pointing in the flow direction. The fluid motion, then, can be described by the unsteady incompressible Cauchy equations,

$$\nabla \cdot \boldsymbol{u} = 0, \tag{1}$$

$$\frac{\partial \boldsymbol{u}}{\partial t} + (\boldsymbol{u} \cdot \nabla)\boldsymbol{u} = -\nabla P + \frac{1}{Re} \nabla \boldsymbol{T}, \tag{2}$$

where $\boldsymbol{u}$ is the velocity vector with components $\boldsymbol{u} = (u, v)$ and P is the reduced pressure. This system is closed when we supply a constitutive relation between the stress tensor $\boldsymbol{T}$ and the rate-of-strain tensor $\boldsymbol{D} = \frac{1}{2}\left[\nabla \boldsymbol{u} + (\nabla \boldsymbol{u})^T \right]$. In this paper we focus on fluids whose $\boldsymbol{T}$ depends linearly on $\boldsymbol{D}$ through the relation $\boldsymbol{T} = 2\mu(S)\boldsymbol{D}$, where $S = (2\boldsymbol{D} : \boldsymbol{D})^{1/2}$. While for a Newtonian fluid the dynamic viscosity μ does not depend on the shear rate S, for a non-Newtonian fluid this dependence cannot be ignored and the functional form of $\mu = \mu(S)$ changes with the particular fluid considered. We adopt a Carreau model that is characterized

by the following viscosity law (Bird *et al* (1987), chapter 4)

$$\frac{\mu - \hat{\mu}_\infty}{\hat{\mu}_0 - \hat{\mu}_\infty} = \left[1 + (\lambda S)^2 \right]^{\frac{n-1}{2}}, \tag{3}$$

where $\hat{\mu}_\infty$ and $\hat{\mu}_0$ are the viscosities at infinite and zero shear rates (the ratio $\hat{\mu}_\infty/\hat{\mu}_0$ is set to 10^{-3}), the parameter n is the power index and λ is the relaxation time.

Equations (1) and (2) are made dimensionless using the cavity depth D as the characteristic length scale, the velocity of the incoming uniform stream U_∞ as the reference velocity and $\hat{\mu}_0$ as the reference dynamic viscosity. Thus, the Reynolds number can be expressed as $Re = \rho U_\infty D/\hat{\mu}_0$. Finally, the system of differential equations (1) and (2) is closed with the following boundary conditions: $\boldsymbol{u} = 1 \cdot \boldsymbol{e}_x$ at the inlet $\partial \mathscr{D}_{in}$, the outflow boundary condition (i.e. $P = 0$, $\partial_x u = 0$) at the outlet $\partial \mathscr{D}_{out}$, no-slip conditions $\boldsymbol{u} = \boldsymbol{0}$ on the solid walls $\partial \mathscr{D}_w$ (represented with a solid line in figure 1), free-slip condition with zero tangential stress (i.e. $\partial_y u = 0$ and $v = 0$) on the upper limit of the computational domain $\partial \mathscr{D}_{ext}$ and on the remaining boundary $\partial \mathscr{D}_{fs}$. Similar conditions are used, for the same reference geometrical configuration, by Sipp and Lebedev (2007) and Barbagallo *et al* (2009).

2.1. Global stability analysis

The instability onset is studied within the framework of the linear stability theory with a classical normal-mode analysis. The stability analysis relies on the existence of a steady solution about which infinitesimal unsteady perturbations are superimposed. The velocity and pressure fields are decomposed into a 2D base flow $\boldsymbol{Q}_b(x, y) = (\boldsymbol{u}_b, P_b)^T = (u_b, v_b, 0, P_b)^T$ and a three-dimensional (3D) disturbance flow, denoted by $\boldsymbol{q}'(x, y, z, t) = (\boldsymbol{u}', P')^T = (u', v', w', P')^T$ of small amplitude ϵ. Introducing this decomposition into (1) and linearizing, we obtain two problems describing the spatial structure of the base flow and the evolution of the unsteady perturbation field. In particular, the base flow is governed by the steady version of (1), whereas the perturbed field is described by the following set of linearized unsteady Carreau equations (uCE)

$$\frac{\partial \boldsymbol{u}'}{\partial t} + \boldsymbol{C}\left\{ \boldsymbol{u}_b, Re \right\} \boldsymbol{u}' = -\nabla P', \tag{4}$$

$$\nabla \cdot \boldsymbol{u}' = 0, \tag{5}$$

where the linearized operator $\boldsymbol{C}$ can be written as

$$\boldsymbol{C}\left\{ \boldsymbol{u}_b, Re \right\} \boldsymbol{u}' = \boldsymbol{u}_b \cdot \nabla \boldsymbol{u}' + \boldsymbol{u}' \cdot \nabla \boldsymbol{u}_b$$

$$- \frac{1}{Re} \nabla \cdot \left[\mu_b \left(\nabla \boldsymbol{u}' + (\nabla \boldsymbol{u}')^T \right) + \mu' \left(\nabla \boldsymbol{u}_b + \left(\nabla \boldsymbol{u}_b \right)^T \right) \right].$$

In the previous definition we have introduced μ_b and μ' that represent the base flow viscosity and the perturbation viscosity, respectively (see e.g. Lashgari *et al* (2012)).

As the base flow is homogeneous in the spanwise direction, a general perturbation can be decomposed into Fourier modes with spanwise wavenumber β. The 3D perturbations may be expressed as

$$\boldsymbol{q}'(x, y, z, t) = \frac{1}{2} \left\{ \left(\hat{\boldsymbol{q}} \right)^T (x, y) \; exp\left[i\beta z + \gamma t \right] + c.c. \right\}, \tag{6}$$

where $\gamma = \sigma + i\omega$ is the angular frequency, $c.c.$ stands for the complex conjugate of the preceding expression and $\hat{\boldsymbol{q}} = (\hat{u}, \hat{v}, \hat{w}, \hat{P})$. Complex conjugation is required in (6) since $\boldsymbol{q}'$ is

real. The angular frequency γ is a complex number: its real part σ represents the temporal growth rate and its imaginary part ω the frequency of the perturbation. The physical meaning of σ is in agreement with the classical definition of stability: for $\sigma > 0$, the base flow is unstable whereas for $\sigma < 0$ it is stable. Introducing the ansatz (6) in (4- 5) that govern the evolution of the perturbation, we obtain a generalized eigenvalue problem that is expressed by means of the following formal relation

$$\mathscr{A}\hat{\mathbf{q}} + \gamma\mathscr{B}\hat{\mathbf{q}} = 0, \tag{7}$$

in which $\mathscr{A}$ is the complex linearized evolution operator. The boundary conditions associated with (7) are derived from those used for the base flow calculation, as in Sipp and Lebedev (2007). Finally, we underline that the two complex eigenpairs $(\sigma + i\omega; \hat{\mathbf{q}})$ and $(\sigma - i\omega; \hat{\mathbf{q}}^*)$ associated with a particular base flow $\boldsymbol{Q}_b$ are simultaneously a solution of the eigenproblem together with the boundary conditions. Thus, the eigenvalues are complex conjugates and the generic spectra in the (σ, ω) plane is symmetric with respect to the real axis.

2.2. Structural sensitivity and the adjoint field

In this section we introduce, in a concise manner, the analysis regarding structural sensitivity. The idea of this analysis is the concept of 'wavemaker' that was introduced by Giannetti and Luchini (2007) and Hill (1992) to identify the location of the core of a global instability (see e.g. Pralits *et al* (2010)). Recently, Luchini and Bottaro (2014) reviewed the use of adjoint equations in hydrodynamic stability analysis. They discussed in detail the adjoint-based sensitivity analysis (Appendix A, Section 9) that is able to map the structural sensitivity of a global oscillator. We refer to this paper for further details.

In Lashgari *et al* (2012) it is shown, using a perturbation analysis, that for each considered global mode $(\sigma + i\omega; \hat{u}, \hat{v}, \hat{w}, \hat{p})$, by adding a forcing term in the form of a (2×2) coupling matrix $\delta\boldsymbol{M}_0$, the following eigenvalue drift is obtained

$$\delta\gamma = \boldsymbol{S}: \delta\boldsymbol{M}_0 = \sum_{ij} S_{ij}\delta M_{0ij}, \tag{8}$$

where we have introduced the sensitivity tensor

$$\boldsymbol{S}(x_0, y_0) = \frac{\hat{\boldsymbol{f}}^+(x_0, y_0)\hat{\boldsymbol{u}}(x_0, y_0)}{\int_{\mathscr{D}} \hat{\boldsymbol{f}}^+ \cdot \hat{\boldsymbol{u}}dS}. \tag{9}$$

The adjoint field $\hat{\boldsymbol{f}}^+$ is obtained using the Lagrange identity (as in Giannetti and Luchini (2007)); thus, the vector field $\hat{\boldsymbol{g}}^+(x, y) = (\hat{\boldsymbol{f}}^+, \hat{m}^+)$ satisfies the following problem:

$$-\gamma\hat{\boldsymbol{f}}^+ + \boldsymbol{C}^+\left\{\boldsymbol{u}_b, Re\right\}\hat{\boldsymbol{f}}^+ + \nabla\hat{m}^+ = 0, \tag{10}$$

$$\nabla \cdot \hat{\boldsymbol{f}}^+ = 0. \tag{11}$$

in which the operator $\boldsymbol{C}^+$ is defined as

$$\boldsymbol{C}^+\left\{\boldsymbol{u}_b, Re\right\}\hat{\boldsymbol{f}}^+ = \boldsymbol{u}_b \cdot \nabla\hat{\boldsymbol{f}}^+ - \boldsymbol{u}^+ \cdot \nabla\boldsymbol{u}_b$$

$$+ \frac{1}{Re}\left[\mu_b\left(\nabla\hat{\boldsymbol{f}}^+ + \left(\nabla\hat{\boldsymbol{f}}^+\right)^T\right) + \left(\nabla\boldsymbol{u}_b + \left(\nabla\boldsymbol{u}_b\right)^T\right) \cdot \nabla\hat{\boldsymbol{f}}^+ V(\boldsymbol{u}_b)\right]$$

where the viscosity fluctuation operator $\boldsymbol{V}$ can be expressed in tensorial notation (see e.g. Lashgari *et al* (2012))

Table 1. Comparison of the results obtained by the present code with those obtained by Sipp and Lebedev (2007) with the meshes $\mathcal{D}1$ and $\mathcal{D}2$. The eigenfrequency ω and growth rate σ have been calculated for the first 2D unstable eigenmode at $Re = 4140$. We report also the number of degrees of freedom ($n_{d.o.f.}$) and the number of triangles (n_t) for each unstructured Mesh.

Mesh	σ	ω	$n_{d.o.f.}$	n_t
$\mathcal{M}1$	0.0007590	7.4931	998668	221045
$\mathcal{M}2$	0.0008344	7.4937	1416630	313791
$\mathcal{M}3$	0.0009122	7.4943	2601757	576887
$\mathcal{D}1$	0.0007401	7.4930	880495	194771
$\mathcal{D}2$	0.0008961	7.4942	1888003	418330

$$V_i(\boldsymbol{u_b}) = 2\left[\frac{\partial\mu}{\partial S_{i1}}(\boldsymbol{u_b})\frac{\partial}{\partial x} + \frac{\partial\mu}{\partial S_{i2}}(\boldsymbol{u_b})\frac{\partial}{\partial y} + \frac{\partial\mu}{\partial S_{i3}}(\boldsymbol{u_b})\frac{\partial}{\partial z}\right]. \tag{12}$$

The boundary conditions associated with the adjoint problem are derived from those used for the direct eigenproblem. Different norms of the tensor $\boldsymbol{S}$ can be used to build a spatial map of the sensitivity. The spectral norm is chosen here to study the worst possible case.

3. Numerical method and validation

3.1. Base flow calculation

The numerical computations of base flow have been performed using a finite element code. In particular, we first derive the associated variational formulation of the Cauchy system (1) and then use the FreeFem ++ (http://www.freefem.org) software to obtain a spatial discretization onto classical $P2 - P1$ Taylor–Hood elements. The resultant nonlinear system of algebraic equations, along with their boundary conditions, is solved with a Newton–Raphson procedure: starting from an initial guess $w_b^{(0)}$, at each step the linear system

$$CE\left(Re, W_b^{(n)}\right) \cdot w_b^{(n)} = -rhs^{(n)} \tag{13}$$

is inverted using the MUMPS-MUltifrontal Massively Parallel sparse direct Solver (Amestoy *et al* (2006, 2010)) and the base flow is then updated as

$$W_b^{(n+1)} = W_b^{(n)} + w_b^{(n)}. \tag{14}$$

The initial guess is chosen as the solution of the Stokes equations and the process is carried out until the L^2-norm of the residual of the governing equations becomes smaller than 10^{-12}. Three different meshes: $\mathcal{M}1$, $\mathcal{M}2$ and $\mathcal{M}3$, have been generated (see table 1) with the Bidimensional Anisotropic Mesh Generator (BAMG) that is present in the Freefem ++ software.

3.2. Eigenvalue solver

Once the base flow is determined, the system (7) is used to perform stability analysis. After spatial discretization, equation (7) along with the boundary conditions are recast in the following standard form

$$\left[A\left(Re,\, W_b \right) + \gamma B \right] \cdot w = \mathbf{0}, \tag{15}$$

where w is the right (or direct) eigenvector. The large number of degrees of freedoms prohibits direct matrix methods and suggests the use of iterative techniques. This means, for example, that methods based on the QR decomposition are not appropriate for solving these large scale problems. Thus, we have chosen to adopt an efficient matrix-free iterative method based on the Arnoldi algorithm (see e.g. Arnoldi (1951)). We use the state-of-the-art ARPACK code of Lehoucq *et al* (1998), which implements the Arnoldi method with implicit restarts to limit memory requirements and to compress the information of the desired eigenvectors into a small subspace. The solutions of the linear systems (15) are determined by the use of the same sparse solver (MUMPS) used for the base flow calculations. The adjoint modes are computed as left eigenvectors of the discrete systems derived from the discretization of the linearized equations and the sensitivity function is then computed by the product of the direct and the adjoint fields. In this paper the right (direct) and left (adjoint) eigenvectors are normalized by requiring

$$\max_{x,y \in \mathscr{D}} \left\{ \left| \hat{u}(x,\, y) \right| \right\} = 1, \quad \int_{\mathscr{D}} \hat{f}^+ \cdot \hat{u} \; dS = 1. \tag{16}$$

3.3. Code validation

In order to perform an accurate validation of the present code (Freefem ++ code) we compare our results with three different test cases. First of all, we validate the stability analysis against the results reported by Sipp and Lebedev (2007). These authors investigate the stability of a Newtonian fluid in the present reference geometrical configuration and report as first instability a 2D eigenmode that becomes unstable at $Re = 4140$. Table 1 compares our results obtained with different meshes ($\mathcal{M}1$, $\mathcal{M}2$, $\mathcal{M}3$) and the results obtained in Sipp and Lebedev (2007). In these particular representative runs, 50 eigenvalues were obtained, with an initial Krylov basis set of dimension 150, and the convergence criterion present in the Arnoldi iterations is based on a tolerance of 10^{-12}. The accuracy of the converged eigenpairs was then independently checked by evaluating the residual $max_i|(A_{i,j} + \gamma B_{i,j})w_j|$, and this quantity was always less than 10^{-9} for the reported results. More importantly, for the leading few eigenpairs, this residual was generally less than 10^{-12}.

We then validated the base-flow velocity profiles (not shown here for sake of brevity) relative to the non-Newtonian channel flow with Nouar *et al* (2007), and an excellent agreement was found. Finally, we compared the stability results for the classical lid-driven cavity problem with those obtained by Haque *et al* (2012). Figure 3 shows the perfect agreement in the computation of the critical Reynolds number for several non-Newtonian flows. In the present work we used the Mesh $\mathcal{M}2$ to perform all computations.

4. Results

First of all, we show the effect of the shear-dependent viscosity on the spatial distribution of the base flow in figure 2. The shear layer that develops above the cavity presents a characteristic wall-normal length scale that increases as the power index n increases. In figure 4 there are displayed several profiles of velocities $u_b(y)$ and $v_b(x)$ inside the cavity for the Newtonian critical Reynolds number $Re = 1370$. In order to determine the influence of the time constant λ on the structure of the base flow, we have chosen to take the parameter n
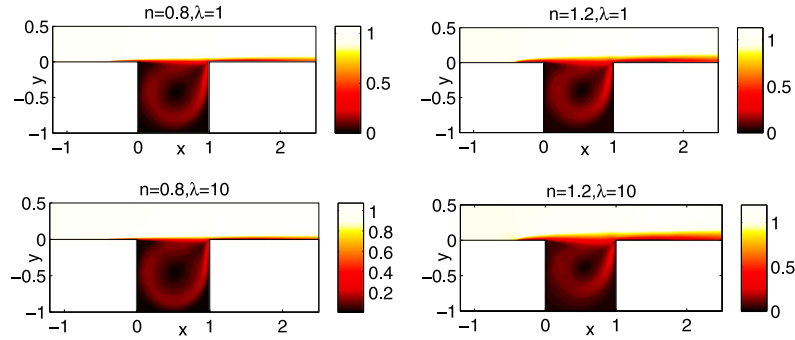
Figure 2. Spatial distribution of the base flow for several values of the parameters λ and n at constant Reynolds number $Re = 1370$. The distribution is displayed through contour plots of the velocity field modulus.
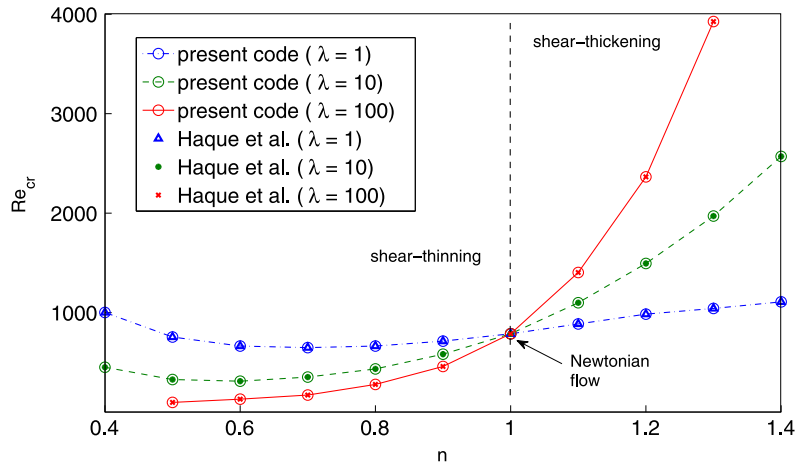

Figure 3. Determination of the critical Reynolds number Re_{cr} for several non-Newtonian lid-driven cavity flows. Comparison of the present stability results with Haque *et al* (2012).

constant and equal to 0.8. The spatial distribution of the profiles suggests that the viscosity parameter λ does not change significantly with the base flow structure inside the cavity.

The dependence of the eigenvalues on the Reynolds number and spanwise wavenumber β is presented in figure 5. In figure 5(a) we show the growth rate (real part σ) of the leading eigenvalues (i.e. the least stable) as a function of the power index n. Compared to the Newtonian fluid, shear-thickening is increasingly stable as the value of n is increased, while this monotonic behaviour is not true for the case of shear-thinning fluids. Figure 5(b) shows the optimal spanwise wavenumber β_{opt} (the value of β corresponding to the neutral curve) as a function of the parameter n. All the curves present a discontinuity in $n \simeq 1.25$ and, consequently, the wavelengths $\hat{\Lambda} = 2\pi / \beta_{opt}$ associated with the corresponding global modes increase from $\hat{\Lambda}_s = \mathcal{O}(0.4)$ (steady modes) to $\hat{\Lambda}_u = \mathcal{O}(1.5)$ (unsteady modes). We have investigated wavenumbers larger than those shown in figure 5b) and find no evidence of other
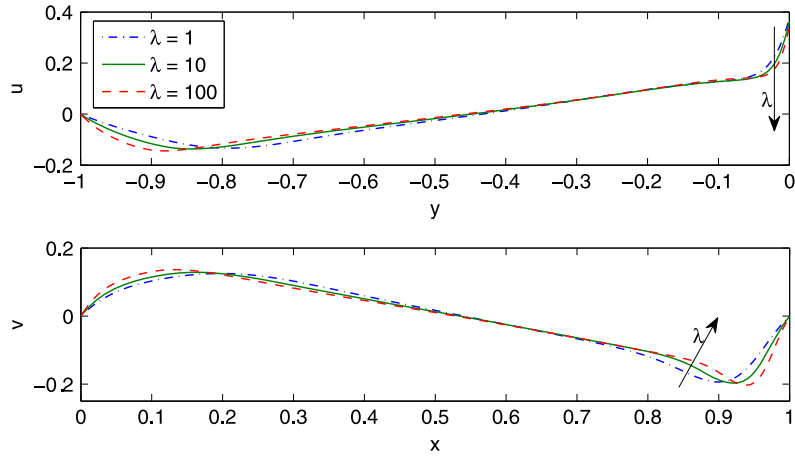
Figure 4. Velocity profiles inside the square cavity: (top) streamwise velocity component u_b at $(x, -0.5)$, (bottom) cross-stream component v_b at $(0.5, y)$. The Reynolds number is $Re = 1370$ and $n = 0.8$
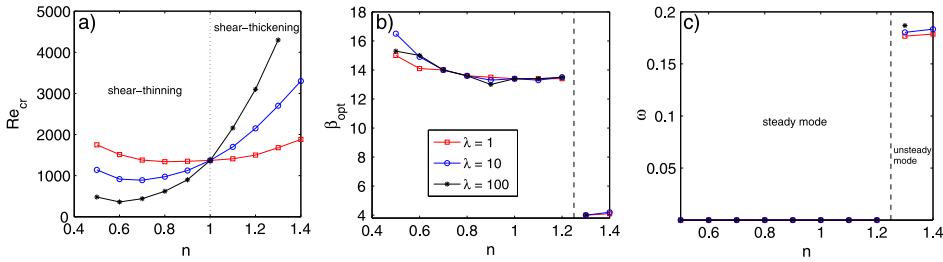

Figure 5. (a) Critical Reynolds numbers as a function of the power index n, (b) corresponding spanwise wavenumbers β (denoted optimal wavenumber) and (c) eigenfrequencies ω.

eigenvalues that would give rise to instabilities for the Reynolds numbers considered. Figure 5(c) shows the associated frequencies of the global modes. Thus, we note that the first absolute linear instability of the steady base flow is a steady or unsteady 3D bifurcation depending on the value of the power-law index n. We note that this behavior is qualitatively the same as in the case of the lid driven cavity flow (see Haque *et al* (2012)).

     The data in figure 5 has been further analyzed in order to investigate if a universal scaling exists for the neutral curve. For this purpose we introduced the averaged Reynolds number, as defined in Haque *et al* (2012) based on the mean viscosity ($Re_{avg.} = \frac{1}{Area} \int Re\,(x, y)\,dxdy$), and plotted the neutral curve as a function of n and λ. The results are presented in figure 6. Indeed it is found that this scaling gives neutral curves that are rather independent of the values of n and λ, when compared to the case of Newtonian fluids ($n = 1$).

     So far only the optimal spanwise wavenumber has been shown for a given Reynolds number. In figure 7 we present the growth rate as a function of the spanwise wavenumber for three values of the power index n and the Reynolds number chosen such that at least one
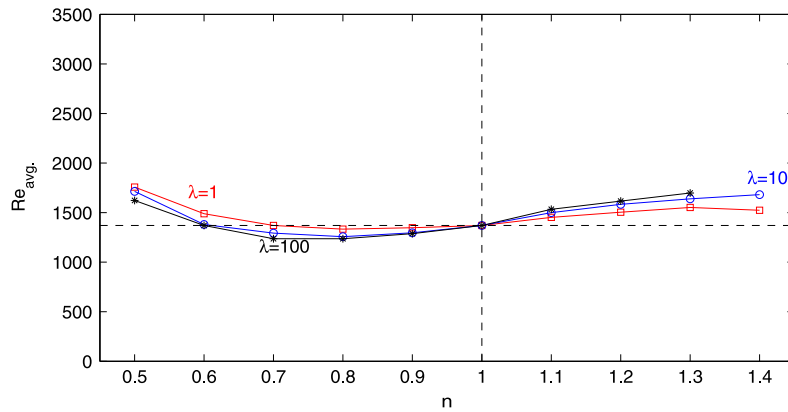
Figure 6. Rescaled neutral curve: the data in figure 5 has been rescaled using the definition of the averaged Reynolds number as found in Haque *et al* (2012).
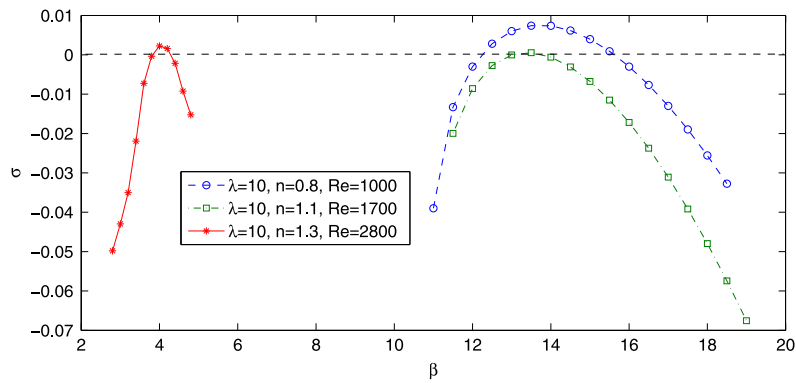

Figure 7. The growth rate σ as a function of the spanwise wavenumber β for different values of the power index n and Reynolds numbers. The value of $\lambda = 10$.

solution is unstable. In all cases $\lambda = 10$. A clear difference in the value of β for the unstable solutions is found passing from $n = 1.1$ to $n = 1.3$.

We now turn to the analysis of the linear modes that destabilize the 2D base flow. Since we want to analyze the features of both steady and unsteady modes, we select as representative cases the flows characterized by $\lambda = 10$, $n = 0.8$ (steady case) and $\lambda = 10$, $n = 1.3$ (unsteady case). Figure 8 shows the structure of the two leading eigenmodes at the respective critical Reynolds numbers and corresponding optimal spanwise wavelengths. The streamwise velocity (figure 8(a)), wall-normal velocity (figure 8(b)) and spanwise velocity (figure 8(c)) contours clearly show that the steady bifurcating mode is localized in the region inside the cavity.

In order to characterize the physical mechanism that underlies the instability, we show in figure 9 a fictitious 3D field obtained as $Q_b + \epsilon q'$. Since the 3D global mode weakly affects the flow outside the cavity, we represent the spatial structure of the field by three streamlines inside the cavity (plotted with solid lines in figure 9). The spatial distribution of the boundary layer developing over the cavity is also visualized by an iso-surface of streamwise velocity
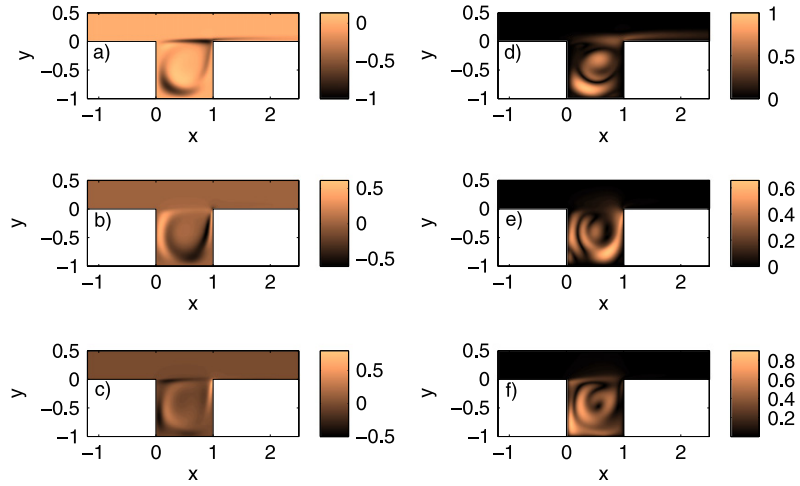
Figure 8. (a–c) Contour plots of the streamwise (a) $\hat{u}(x, y)$, wall-normal (b) $\hat{v}(x, y)$ and spanwise (c) $\hat{w}(x, y)$ direct eigenfunction of the steady mode: $Re_{cr} = 970$, $\beta_{opt} = 13.6$, $\lambda = 10$ and $n = 0.8$. (d–f) Visualization of the structure of direct eigenfunction of the non-stationary mode by contours of modulus of streamwise (d) $|\hat{u}(x, y)|$, wall-normal (e) $|\hat{v}(x, y)|$ and spanwise (f) $|\hat{w}(x, y)|$ component: $Re_{cr} = 2700$, $\beta_{opt} = 4$, $\lambda = 10$ and $n = 1.3$.

and the streamwise structure of the flow is depicted by three slices. Thus, the secondary flow generated by this instability can be described as flat rolls lying inside the cavity similar to those reported by the 3D linear instability of the lid-driven cavity flow (see Albensoeder *et al* (2001)). Figure 9 is made by taking the optimal Fourier wavelength as the transverse length. The first unsteady mode, instead, is displayed in figure 8(e–g) by the modulus of the three components $\hat{u}$, $\hat{v}$ and $\hat{w}$. The dynamics associated with this mode are a periodic oscillation concentrated in the region inside the cavity. The secondary flow generated in this case has a more complicated spatial structure with several 'rolls' but again localized within the cavity. The exact size and shape of the cavity vortex depends weakly on the global flow properties, so, the 3D instabilities, driven by this local part of the flow field, always present similar features. The receptivity behavior of the steady and unsteady mode is then investigate by an adjoint analysis. In figure 10 is reported the spatial structure of the adjoint field using the contours of the modulus of the adjoint velocity. For the stationary mode (figure 10(a)) the receptivity to a momentum forcing is strong both near the right wall of the cavity and very close to the left edge. The unsteady mode (figure 10(b)) presents the same receptive behavior with a slight difference in the distribution of the maximum of the field. We have to note that the region of high receptivity located on the left corner is the main difference with the lid-driven cavity case.

Finally, following Chomaz (2005) and Giannetti and Luchini (2007), we have examined the sensitivity of the leading eigenvalue to structural perturbations of the linear evolution operator in order to determine the region of the flow where feedback processes at the origin of a self-sustained instability are active. In figure 11 we show the structural sensitivity map for both the unsteady and steady mode. In physical terms, this overlap region identifies where local feedback will have a large impact on the leading eigenvalue. The sensitivity associated with the steady mode (figure 11(a)) and with the unsteady mode (figure 11(b)) again have a
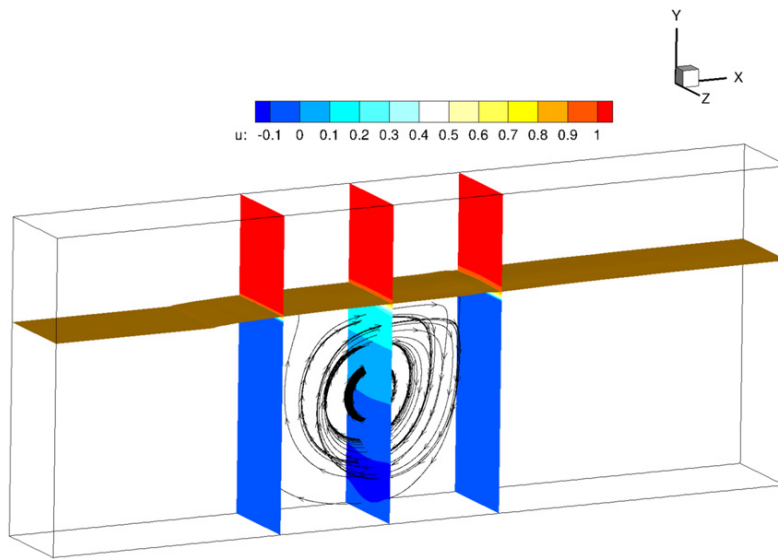
Figure 9. Perspective view of the secondary flow generated by the steady bifurcating mode ($Re_{cr} = 970$, $\beta_{opt} = 13.6$, $\lambda = 10$ and $n = 0.8$). The total field is obtained as $\boldsymbol{Q_b} + \epsilon\boldsymbol{q}'$ where the small amplitude ϵ of the perturbation field is set to $\epsilon = 0.05$. Threeslices are placed respectively at $x = 0$, in the middle of the cavity ($x = 0.5$) and at $x = 1$. The structure of the shear layer developing above the cavity is visualized by an iso-surface of the streamwise component of total velocity U (iso-surface value = 0.9). The spatial distribution of the total field is displayed within the cavity with three streamlines.
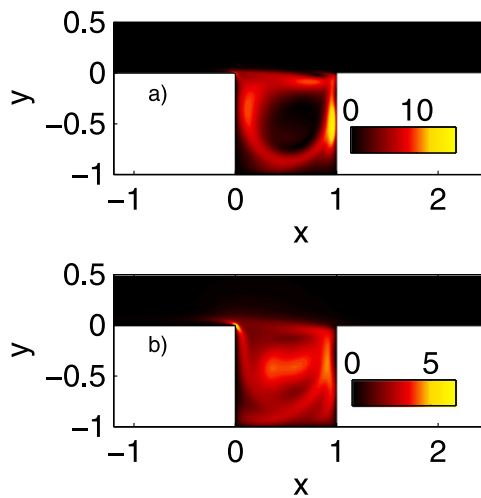

Figure 10. Contour plots of the modulus of the adjoint field for the (a) steady mode ($Re_{cr} = 970$, $\beta_{opt} = 13.6$, $\lambda = 10$ and $n = 0.8$) and (b) unsteady mode ($Re_{cr} = 2700$, $\beta_{opt} = 4$, $\lambda = 10$ and $n = 1.3$).

Figure 11. Visualization of the structural sensitivity for the (a) steady mode ($Re_{cr} = 970$, $\beta_{opt} = 13.6$, $\lambda = 10$ and $n = 0.8$) and (b) unsteady mode ($Re_{cr} = 2700$, $\beta_{opt} = 4$, $\lambda = 10$ and $n = 1.3$).
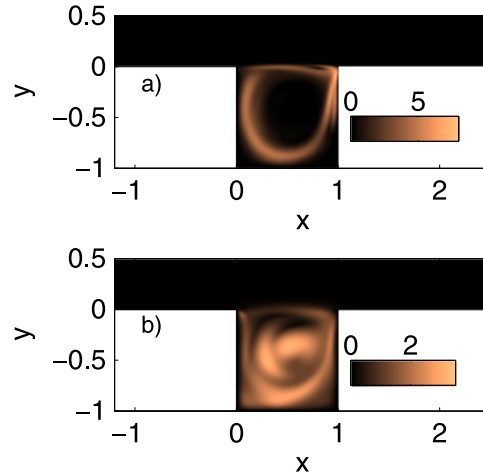
similar structure concentrated only inside the cavity. Thus, any local feedback applied outside this region only slightly modifies the leading eigenvalue, indicating that these regions do not play a significant role in the process giving rise to global instability. For the present flow configuration, we may conclude that the cavity vortex is the wavemaker region of the 3D instability for both modes.

5. Conclusions

In this paper we have presented the linear dynamics of a 2D flow arising in open cavity configurations for the case of non-Newtonian fluids given by the Carreau viscosity model. A global stability analysis has been performed in order to map the neutral stability curves as a function of the Reynolds number, and the model parameters n and λ. We have found that the primary bifurcation is always 3D but can have both steady or non-stationary behavior, depending on the value of the power index n. In particular, a single value of $n \approx 1.25$ separates the steady and unsteady bifurcations.

A detailed analysis of the structure of both leading global modes suggest that the instability is localized within the cavity. Furthermore, we have computed the adjoint global modes associated with the respective direct mode in order to show the receptive behavior of the base flow. An analysis of the adjoint spatial structure allowed us to localize two regions of strong receptivity to momentum forcing. The direct and adjoint modes are all concentrated inside the cavity in the same region. Thus, the overlap field is again localized within the cavity. We have further shown that if the Reynolds number is based on the average viscosity (as in Haque *et al* (2012)), a more or less universal value of the critical Reynolds number is found, independent of both n and λ. Finally, we conclude that the results summarized above suggest the same instability mechanism of the lid-driven cavity flow.

References

Albensoeder S, Kuhlmann H C and Rath H J 2001 3D centrifugal-flow instabilities in the lid-driven-cavity problem *Phys. Fluids* **13** 121–35

Amestoy P R, Duff I S, Koster J and L'Excellent J-Y 2010 A fully asynchronous multifrontal solver using distributed dynamic scheduling *SIAM Journal on Matrix Analysis and Applications* **23** 15–41

Amestoy P R, Guermouche A, L'Excellent J-Y and Pralet S 2006 Hybrid scheduling for the parallel solution of linear systems *Parallel Computing* **32** 136–56

Arnoldi W E 1951 The principle of minimized iteration in the solution of the matrix eigenproblem *Quart. Appl. Math.* **9** 17–29

Barbagallo A, Sipp D and Schmid P J 2009 Closed-loop control of an open cavity flow using reduced-order models *J. Fluid Mech.* **641** 1–50

Bird R B, Curtiss C F, Armstrong R C and Hassager O 1987 *Dynamics of Polymeric Liquids* vol 1, 2nd edn (New York: Wiley-Interscience)

Brandt L, Sipp D, Pralits J O and Marquet O 2011 Effect of base-flow variation on non-modal stability *J. Fluid Mech.* **687** 503–28

Brés G A and Colonius T 2008 3D instabilities in compressible flow over open cavities *J. Fluid Mech.* **599** 309–39

Carreau P J, Dekee D and Chhabra R P 1997 *Rheology of polymeric systems* (Munich: Hanser)

Chomaz J M 2005 Global instabilities in spatially developing flows: non-normality and nonlinearity *Annu. Rev. Fluid Mech.* **37** 357–92

Cochrane T, Walters K and Webster M F 1981 On Newtonian and non-Newtonian flow in complex geometries, Phil. Trans *Soc. Lond.* A **301** 161–81

Giannetti F and Luchini P 2007 Structural sensitivity of the first instability of the cylinder wake *J. Fluid Mech.* **581** 167–97

Haque S, Lashgari I, Giannetti F and Brandt L 2012 Stability of fluids with shear-dependent viscosity in the lid-driven cavity *J. Non-Newtonian Fluid Mech.* **173-174** 49–61

Hill D C A 1992 theoretical approach for analysing the restabilization of wakes *NASA Technical Memorandum* (Moffett, CA) 103858

Hsu C-H, Vu H-H and Kang Y-H 2009 The Rheology of Blood Flow in a Branched Arterial System with 3D Model: A Numerical Study *Journal of Mechanics* **25** 21–24

Lashgari I, Pralits J O, Giannetti F and Brandt L 2012 First instability of the flow of shear-thinning and shear-thickening fluids past a circular cylinder *J. Fluid Mech.* **701** 201–27

Lehoucq R B, Sorensen D C and Yang C 1998 *ARPACK User's. Guide: Solution of Large Scale Eigenvalue Problems With Implicityly Restarted Arnoldi Methods* (SIAM)

Luchini P and Bottaro A 2014 Adjoint Equations in Stability Analysis *Annu. Rev. of Fluid Mech.* **46** 493–517

Marquet O, Sipp D and Jacquin L 2008 Sensitivity analysis and passive control of cylinder flow *J. Fluid Mech.* **615** 221–52

Nouar C, Bottaro A and Brancher J P 2007 Delaying transition to turbulence in channel flow: revisiting the stability of shear-thinning fluids *J. Fluid Mech.* **592** 177–94

Pralits J O, Brandt L and Giannetti F 2010 Instability and sensitivity of the flow around a rotating circular cylinder *J. Fluid Mech.* **650** 513–36

Pralits J O, Giannetti F and Brandt L 2013 Three-dimensional instability of the flow around a rotating circular cylinder *J. Fluid Mech.* **730** 5–18

Rossiter J E 1964 Wind-tunnel experiments on the flow over rectangular cavities at subsonic and transonic speeds *Tech. Rep.* 3438 ARC

Rowley C W, Colonius T and Basu A J 2002 On self-sustained oscillations in 2D compressible flow over rectangular cavities *J. Fluid Mech.* **455** 315–46

Sipp D and Lebedev A 2007 Global stability of base and mean flows: a general approach and its applications to cylinder and open cavity flows *J. Fluid Mech.* **593** 333–58